Biosensors and Bioelectronics 294 (2026) 118163

Contents lists available at ScienceDirect

Biosensors and Bioelectronics

journal homepage: www.elsevier.com/locate/bios

Feasibility of continuous microvascular tissue oxygenation monitoring using discrete optical semiconductor devices ☆

Tuukka Panula [a,*], Inka Mustajoki [a], Tomi Jaakola [a], Tarja Niemi [b], Matti Kaisti [a]

[a] Department of Computing, Faculty of Technology, University of Turku, Turku, 20500, Finland
[b] Department of Plastic Surgery, Turku University Central Hospital, Turku, 20520, Finland

ARTICLE INFO

Keywords:
Oximetry
Tissue perfusion
Microcirculation
Light-emitting diode
Photoplethysmography

ABSTRACT

This study evaluates the potential for the use of low-cost discrete optical semiconductors, specifically light-emitting diodes (LEDs) and a photodiode, for non-invasive measurement of microvascular tissue oxygen saturation (StO_2). StO_2 is a crucial biomarker in monitoring microvascular function and tissue viability. Spectrometer-based methods typically use complex and expensive equipment, with the cost per patient potentially amounting to hundreds of dollars. This study aims to provide understanding of tissue–light interaction with broader implications extending to applications such as photoplethysmography (PPG). Our approach involves a system that includes three specifically selected LEDs coupled with a photodiode, focusing on assessing microvascular StO_2. The methodology includes several phases: *in vitro* calibration using a controlled deoxygenation process in a liquid tissue phantom, computational simulations to estimate the penetration depths of selected LED wavelengths, an analysis of the effects of variability in LED output on measurement accuracy, and a preliminary human study. Results from the *in vitro* experiments demonstrated a root mean square error of 3.9 StO_2-% between a spectrometer reference and our technique. The human study including baseline, occlusion and post-occlusion StO_2 measurements in six volunteers resulted in 76.0, 52.6 and 77.5 StO_2-%, respectively. Computational simulations confirmed the effective penetration of selected wavelengths into targeted microvascular layers. The intrinsic and external factors affecting the measurement accuracy were analyzed. The findings support the feasibility of a cost-effective, simplified, and effective system for continuous monitoring of microvascular tissue oxygenation.

1. Introduction

Impaired microvascular function has been associated with the development and progression of various diseases. The relationship between diabetes and microcirculatory dysfunction has been extensively studied and well established. More recently, there has been growing evidence linking microcirculatory dysfunction and cardiovascular diseases (CVD), such as heart failure with preserved ejection fraction (HFpEF) (Strain and Paldánius, 2018; Weerts et al., 2022). Given that microvascular dysfunction is often a systemic condition, with similar pathologies observed across multiple organs, skin microcirculation can serve as a valuable proxy for microvascular health in other tissues (Feuer et al., 2022). Importantly, skin also allows for non-invasive measurement.

Tissue oxygen saturation (StO_2) is an essential biomarker for assessing oxygen delivery and consumption in the microvasculature. StO_2 is closely related to the commonly used peripheral oxygen saturation (SpO_2) measured by pulse oximetry. SpO_2 is often used as a surrogate marker to assess systemic oxygen saturation, while StO_2 can be used to monitor local microvascular tissue oxygenation. Unlike SpO_2, the measurement of StO_2 involves selecting specific wavelengths and source–detector configurations that target only the superficial tissue layers associated with the microvasculature. Superficial StO_2 measured by lower wavelengths is called microvascular StO_2, where majority of the signal consists of arteriolar and capillary oxygenation. For computing StO_2, the non-pulsatile (DC) components of the measured photoplethysmographic (PPG) signals are used. The DC component is not related to the cardiac cycle but rather to the quasi-static properties of the underlying tissue, such as the concentration of chromophores. Since StO_2 computation does not rely on pulsatile components it is also suited for measuring ischemic regions, unlike SpO_2 (Pickett et al., 1997; Jubran, 1999).

☆ This article is part of a Special issue entitled: 'Continuous Monitoring Biosensors' published in Biosensors and Bioelectronics.

* Correspondence to: Vesilinnantie 5, 20500 Turku, Finland.
E-mail address: tuukka.j.panula@utu.fi (T. Panula).

https://doi.org/10.1016/j.bios.2025.118163
Received 19 September 2025; Received in revised form 22 October 2025; Accepted 26 October 2025
Available online 4 November 2025

A well-established application of StO_2 is the evaluation of tissue perfusion following revascularization in microvascular flap surgery (Dat et al., 2017). Free microvascular tissue reconstruction is widely used to repair defects caused by trauma or various types of cancer surgery, either immediately or at a later stage of treatment. Postoperatively, vascular compromise can lead to flap necrosis. The likelihood of successful salvage is directly proportional to the speed of problem detection and the prompt restoration of circulation (Chae et al., 2015).

Various commercial and academic efforts have been made in StO_2 monitoring. The technical implementation can be approached in two ways: either the light source or the detector must be capable of separating different spectral bands to enable the selection of specific wavelengths. A common implementation is using a high-resolution VIS–NIR spectrometer with a fiber optic probe. This approach requires expensive and bulky optics compared to discrete LEDs and photodetectors. T-Stat 2 (Spectros Medical Devices, USA) is a microvascular StO_2 monitor, which uses a spectrometer with specific wavelengths selected between 476–584 nm (Benaron et al., 2003, 2004). Spectrometer-based approach is also used in OxyVLS (Nasseri et al., 2018). Discrete semiconductor based approaches have been used in various devices as well. Inspectra model 650 (Hutchinson Technology, USA) uses NIR wavelengths to measure StO_2 from the thenar eminence using a fiber optic probe attached to the palm. Wearable devices, both invasive and non-invasive have been proposed previously. A 2019 study used IR and yellow LEDs in a wearable form factor to assess StO_2 (Berthelot et al., 2019). The values were calibrated using a machine learning method. Another study experimented with the usage of a wide-spectrum light source and a RGB color sensor mounted on a flexible substrate. The results showed a response to arterial and venous occlusion but they were unable to assess actual StO_2 (Moreno-Oyervides et al., 2023). Invasive StO_2 monitoring was demonstrated in a study involving the use of red and IR micro LEDs mounted on a flexible probe with bioresorbable barbs (Tomioka et al., 2022). Another invasive approach was proposed in a study using a blue LED along with an oxygen sensing film (Sonmezoglu et al., 2021). While the literature demonstrates increasing efforts in the development of discrete semiconductor-based methods, comprehensive analysis and insight into the fundamental measurement mechanisms are still lacking.

The skin is a particularly interesting site for assessing microcirculation, as its distinct structure features macro- and microcirculatory vessels located in separate subcutaneous layers. Consequently, by adjusting the penetration depth of the light, it is possible to target and assess different levels of the circulatory system. Targeting microvascular blood flow at the very surface of the skin requires the selection of specific spectral windows (Prahl, 1999). A key requirement is sufficient spectral separation between the absorption of oxyhemoglobin and deoxyhemoglobin. Detailed description of the hemoglobin absorption spectra and spectral windows is shown in Supplementary Figure A.6. The penetration depth increases rapidly after approximately 600 nm (Finlayson et al., 2022). In conventional NIRS applications, wavelengths in the range of approximately 650–800 nm and 800–950 nm, corresponding to the absorption spectra of deoxygenated and oxygenated hemoglobin, respectively, penetrate the skin and reach deeper tissues such as muscle. Although deeper StO_2 measurements provide valuable information, they primarily reflect systemic hemodynamic status rather than local microvascular function. In the NIR region, there is considerable flexibility in selecting LED wavelengths, as the available spectral windows are wide. Variations in the peak wavelength of the LED or the spectral width have only a minor influence on the measurement output. However, the same does not apply to the wavelength range of approximately 450–600 nm, which is suitable for superficial probing but exhibits higher spectral variation in hemoglobin absorption. As a result, the usable spectral windows are relatively narrow compared to the NIR region. Importantly, all selected spectral windows should be within the 450–600 nm range to ensure similar penetration depths and confine the measurements to superficial tissue. The suitability of LED-based monitoring, as well as a detailed analysis of wavelength selection, has not been systematically examined in prior studies.

The aim of this study is to assess the feasibility of using LEDs and a photodiode for StO_2 measurement, with the goal of reducing system complexity and cost. Furthermore, miniaturization, along with reduced power consumption, would enable wearable continuous monitoring. To investigate this, we developed a dedicated sensing system. We performed both *in vitro* and *in vivo* measurements and compared the results to those obtained from reference devices. In addition, we used the Monte Carlo method to simulate tissue–light interactions for the proposed setup. We also evaluated how the properties of individual system components affect StO_2 measurement accuracy. In this study, we focus solely on local tissue monitoring approaches, excluding broader applications such as cerebral NIR spectroscopy.

2. Materials and methods

2.1. Device development

The DAQ units 2-layer printed circuit board (PCB) houses a BMD-380-A-R microcontroller module (u-Blox, Switzerland), which is built around the nRF52840 (Nordic Semiconductor, Norway) ARM Cortex-M4 based chipset. The device is powered by two AA batteries and an LTC3526 DC/DC step-up boost converter (Analog Devices, USA) is used to provide stable 3 V operating voltage. Reverse polarity protection is implemented using a SI2323DDS N-channel MOSFET (Vishay Intertechnology, USA). The DAQ unit also houses a MEM2075 MicroSD memory card connector (Global Connector Technology, UK) and two 54-00177 (Tensility International Corporation, USA) 3.5 mm connector jacks. The 3.5 mm jacks are used for I^2C connectivity with the sensor units. IN-S66TBTRGB RGB LED (Inolux, USA) is used to indicate status of the system to the user: blinking green light for an on-going measurement and steady red light in case of a system fault.

The sensor unit PCB has 2-layers and houses the components on both sides. A matte black solder mask was selected in order to minimize reflections from the LEDs. The bottom side of the PCB houses a photodetector (VEMD1060X01, Vishay Intertechnology) as well as three LEDs: APHD1608LVBC/D (Kingbright, Taiwan), APHD1608LSYCK (Kingbright) and SML-D13Y2WT86 (ROHM Semiconductor, Japan), with reported nominal peak wavelengths of 465 nm, 592 nm and 581 nm respectively. All other components are on the top side of the PCB. The LEDs are driven with the KTD2037E constant current 3-channel LED driver (Kinetic Technologies, USA). Each channel output current is individually programmable. The output of the photodiode is amplified using a transimpedance amplifier (TIA) circuit built around the OPA341 operational amplifier (Texas Instruments, USA). The signal is digitized with an ADS1114 (Texas Instruments, USA) 16-bit analog-to-digital converter (ADC) with a passive anti-aliasing filter at the input. To ensure stable operation, both the TIA and the ADC are powered by a 2.5 V voltage source generated by an LT1761 (Analog Devices) linear voltage regulator. The schematic for the optical front-end and the assembled PCB are shown in Fig. 2b and c, respectively.

The microcontroller firmware is responsible for pulsing the LEDs, reading the ADCs and storing the data into the memory card. A measurement is triggered every 10 s and both sensors are read simultaneously. During each measurement cycle, the LEDs are multiplexed and the ADC is read with one LED on at a time. Each LED is sampled at 10 Hz. 1.5 s of data is collected at each cycle resulting in 15 samples for each individual LED. After 5 read cycles, the data is written to the memory card using the FAT file system protocol. The system diagram is shown in Fig. 1a and the assembled device in Fig. 1b.

The enclosures for both the DAQ and sensor units were 3D printed. White resin was used for all other parts than the bottom of the sensor probe, where black resin was used to minimize the effect of ambient light on the measurement. The side attached to the skin is shown in

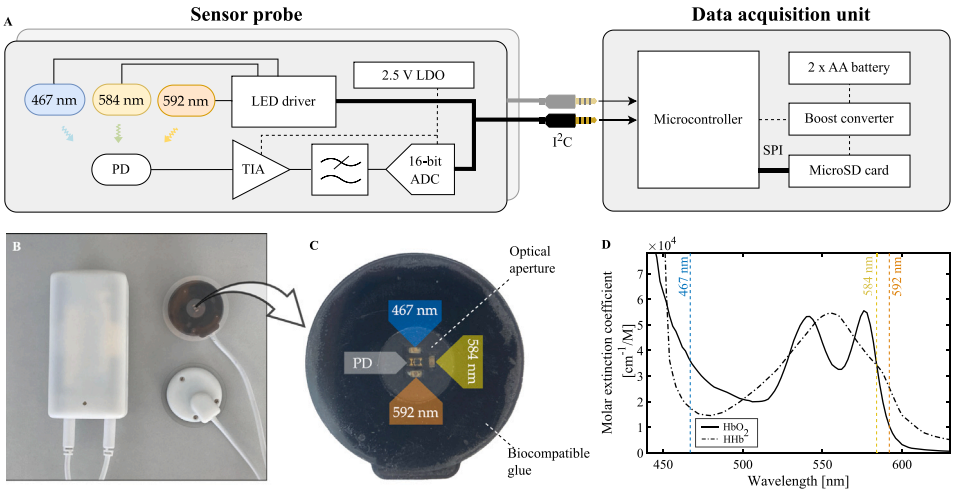

Fig. 1. System description. (a) Block diagram of the system consisting of a main data acquisition unit and two sensor units. (b) Photograph of the instrument. (c) Close-up photograph of the sensor probe, with three LEDs and a photodiode. The custom skin tape has a circular aperture for the optical components. Each component has a separate opening. (d) Absorption spectra of oxyhemoglobin and deoxyhemoglobin. The peak wavelengths of the LEDs have been chosen at specific points in the spectral windows.

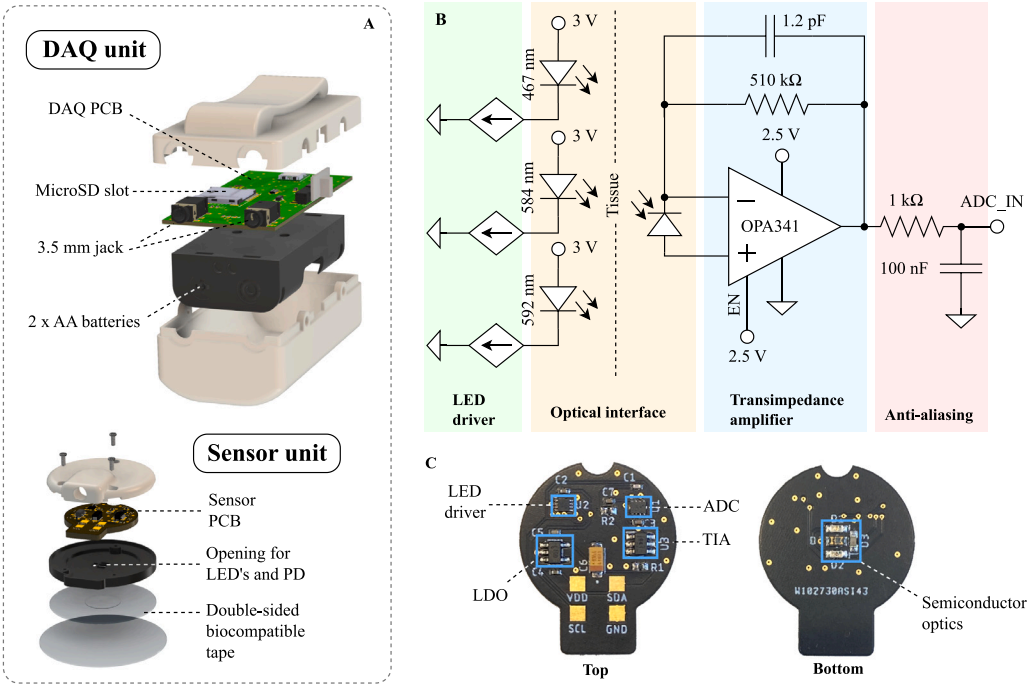

Fig. 2. Device development. (a) 3D renditions of the main data acquisition unit and the sensor probe. (b) Schematic of the optical front-end. (c) Photographs of the sensor probe PCB.

Fig. 1c. The DAQ unit enclosure has an opening and a light guide for the status LED as well as a clip to attach the device to e.g. a patient gown. The probe is attached to the skin via a custom sticker patch. The tape substrate material of the probe is transparent polyethylene terephthalate (PET) plastic with a thickness of 0.5 mm. Both sides are covered with a biocompatible double-sided tape (1522, 3M, USA). A 10 mm diameter area is left without tape to allow good optical coupling with the tissue, yet providing isolation from direct skin-to-electronics contact. An additional PET sheet on both sides is used to protect the tape before use. A 3D rendition of the device is shown in Fig. 2a.

2.2. Reference instruments

InSpectra 650 (Hutchinson Technology, USA) StO_2 oxygenation monitor was used as a reference monitor for the *in vivo* experiments. For the *in vitro* experiments we used a spectrometer setup consisting of a FLAME-T-VIS-NIR-ES (Ocean Insight, USA) visible-to-near-infrared (VIS–NIR) spectroscope, a tungsten halogen light source (HL-2000-HP, Ocean Insight) and a reflection/backscatter probe (QR400-7-VIS-BX, Ocean Insight).

2.3. 3D printing

The enclosures for DUT were 3D printed using Form 3+ (Formlabs, USA) stereolithography (SLA) printer. The sample holder for the liquid phantom was printed with a Raise3D E2 fused deposition modeling (FDM) printer (Raise 3D Technologies, USA).

2.4. Software

The electronics were designed using Autodesk Eagle 9.6.2 electronic design automation (EDA) software. The enclosure was designed with Autodesk Inventor 2024 computer-automated design (CAD) software and prepared for 3D printing with Formlabs PreForm. The device firmware was written in C using Segger Embedded Studio 7.30 integrated development environment (IDE). VIS–NIR spectrometer data was recorded using OceanView graphical user interface (GUI) software. Data analysis and tissue–light interaction Monte Carlo simulation were performed on MATLAB R2024a. *In vitro* VIS–NIR spectrometer data analysis was done on Python v3.12.0.

2.5. Reference StO_2 algorithm

For the reference StO_2 obtained by the VIS–NIR spectrometer we used the well established Knoefel algorithm (Knoefel et al., 1996). White reference was recorded using a diffuse reflectance target. Optical densities (OD) were calculated by:

$$OD^{\lambda} = \log_{10}\left(\frac{I_0}{I}\right)^{\lambda} \tag{1}$$

where I_0 is the white reference intensity, and I is the measured intensity at the desired wavelength λ (Knoefel et al., 1996; Gade and Greisen, 2016; Kleiser et al., 2018).

HbO_2 and HHb values as well as the tissue oxygenation StO_2^{ref} for the VIS–NIR spectrometer were determined using the following equations:

$$[HbO_2] = \frac{OD^{577}\cdot\epsilon^{555}_{deoxy} - OD^{555}\cdot\epsilon^{577}_{deoxy}}{\epsilon^{577}_{deoxy}\cdot\epsilon^{555}_{oxy} - \epsilon^{555}_{deoxy}\cdot\epsilon^{577}_{oxy}} \tag{2}$$

$$[HHb] = \frac{OD^{555} - [HbO_2]\cdot\epsilon^{555}_{oxy}}{\epsilon^{555}_{deoxy}} \tag{3}$$

$$[StO_2^{\mathrm{ref}}] = \frac{[HbO_2]}{[HbO_2] + [HHb]} \tag{4}$$

The extinction coefficients ϵ^{λ} for HbO_2 and HHb at each wavelength were taken from Prahl (1999).

2.6. Liquid phantom experiments (in vitro)

We prepared a liquid phantom that mimics the optical properties of human tissue. The solution contained 82% phosphate-buffered saline (PBS, 806552,Sigma-Aldrich, USA), 0.82% sodium-bicarbonate solution (SBS, S8761, Sigma-Aldrich, USA) for pH stabilization, 8.2% bovine blood (Veljekset Rönkä Oy, Finland) for hemoglobin, and 10% intralipid (20% IL, I141, Sigma-Alrdich, USA) for modifying the optical properties of the solution to be close to human skin tissue. The hemoglobin in the blood was deoxygenated using 1 ml solution containing 0.4% dry yeast and 2% table sugar per 25 ml of blood solution. Approximately 15 ml of blood–yeast solution was used for the measurements. A new solution was prepared for each deoxygenation cycle.

For the measurement, 50 ml polypropylene tubes (Sarstedt, Germany) were used, and the tube was placed into 3D-printed black polylactic acid (PLA) holder to minimize the effect of external light. The spectrometer probe and DUT were covered by Parafilm (Bemis Company, USA).

2.7. Human study (in vivo)

Three brachial occlusion measurements were performed for six subjects resulting in 17 measurements in total. One measurement was discarded due to poor signal quality originating from a loose sensor-to-skin connection. Each measurement consists of approximately 12.5 min of data. The measurements were taken on DUT and the reference device simultaneously. The measurements were taken in a supine position with the two DUT sensor probes in contra-lateral hands. The reference Inspectra sensor was placed on the thenar eminence of the left hand. All sensors were attached on the surface of the palm. In addition, a short 30 s period of spectral data using the VIS–NIR spectrometer was recorded from the right hand at the beginning of each measurement. The measurement was taken by manually placing and holding the probe on the skin next to our probe. A 3D printed holder was used to ensure that the probe remained perpendicular to the skin.

A 5 min baseline was recorded, followed by a 2 min period of brachial occlusion, where the brachial artery was blocked by applying suprasystolic pressure (180–200 mmHg) to the arm cuff of an aneroid sphygmomanometer (R1 Shock Proof, Rudolf Riester GmbH, Germany). After the pressure was released, the recording was continued for another 5 min.

In addition to the occlusion tests, we recorded StO_2 (n=5) during different activities/positions including laying in a supine position (2 x 3 min), laying on the right side (3 min), laying on the left side (3 min), sitting (3 min) and walking (4 min). The measurement also included a 5 min resting period at the beginning. Only the DUT was used and the sensor probes were attached to the left and right side of the chest in order to simulate the monitoring of breast free flap surgery.

Additionally, a proof-of-concept measurement was taken from a post-operative patient in an actual clinical setting in Turku University Hospital. The measurement was done from healthy tissue for a duration of 60 h.

All measurements were conducted according to the Declaration of Helsinki guidelines. Informed consent was obtained from all subjects. The methods were performed in accordance with relevant guidelines and regulations and approved by the Ethical Committee of the Hospital District of Southwest Finland and Finnish Medicines Agency (FIMEA/2024/002778).

2.8. Tissue–light interaction

Tissue–light interaction was simulated with a Monte Carlo (MC) multilayer skin model. In MC-method-based photon propagation simulations, photon packets are launched into the tissue, after which their random walk in the tissue is tracked. Scattering events change the paths of the photon packets, while absorption events change the weight of the packet (Prahl et al., 1989; Wang et al., 1995; Sirkiä et al., 2023). Simulations were performed on MATLAB using the Monte Carlo eXtreme (MCX) light transport simulator. MCX is an open-source Monte Carlo simulation software that uses graphics processing unit threads to simulate photons in parallel Fang and Boas (2009), Yu et al. (2018), Yan and Fang (2020).

Five different wavelengths, 465 nm, 585 nm and 590 nm, 680 nm and 800 nm, closely corresponding to the three wavelengths used in the system and the lowest and highest wavelengths used in the reference device, were simulated for a seven-layer skin model (Sirkiä et al., 2023; Bashkatov et al., 2008). The skin model consists of stratum corneum (thickness = 0.4 mm), living epidermis (0.1 mm), papillary dermis (0.2 mm), upper blood net dermis (0.1 mm), reticular dermis (1.4 mm), deep blood net dermis (0.1 mm), and subcutis (rest of the domain space). Bone was not taken into account in these simulations. The layer-specific values for volume fractions of blood, water, and melanin, refractive indices, and mean inner diameters of blood vessels were adapted from the literature. These are used with the literature values of wavelength-dependent anisotropy factors and absorption and scattering

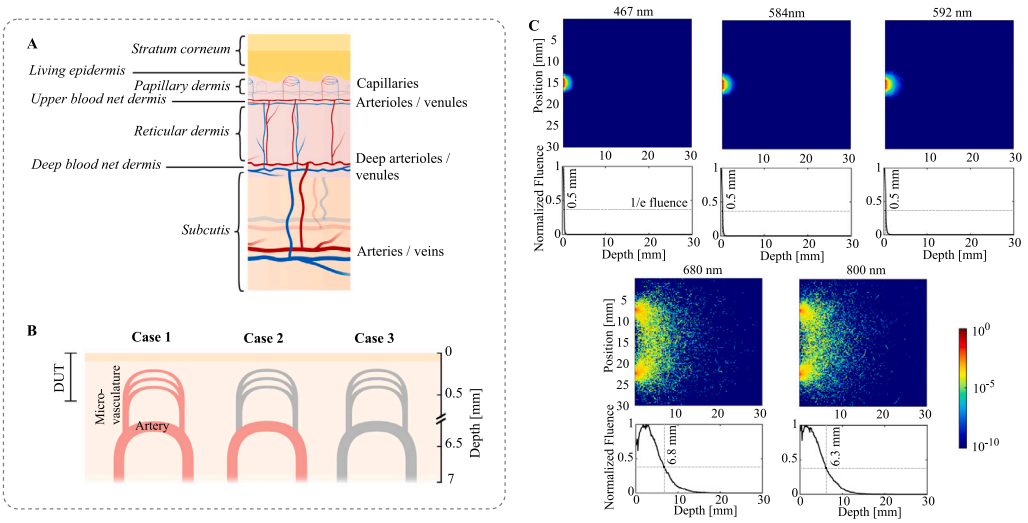

Fig. 3. Tissue–light interaction. (a) Cross-sectional view of skin vasculature. (b) Three cases showing normal perfusion and different layers of impaired circulation. (c) Monte Carlo simulations. The top plots portray the fluence of photon packets emitted from the LED that reach the photodiode. In DUT, the distance between the LED and the PD is 1.7 mm compared to 15 mm in the StO_2 reference device. The bottom plots depict the decrease in fluence as a function of tissue depth. The level of attenuation to 1/e, or 37%, of the maximum value is marked as the penetration depth.

coefficients of different tissue components to calculate the total absorption coefficient μ_a, scattering coefficient μ_s, and anisotropy factor g for each skin layer and for each of the five simulated wavelengths Sirkiä et al. (2023).

The simulations were run in a configuration of 10^9 simulated photons, 300^3 voxel domain with 0.1 mm grid edge length, and pencil beam source type. The source–detector separation was 1.7 mm for 465 nm, 585 nm and 590 nm wavelengths (DUT) and 15 mm for 680 nm and 800 nm (Inspectra) wavelengths. Fluence rate was used to estimate the penetration depth of each wavelength. The attenuation threshold $1/e$ ($\sim$ 37%) of the maximum fluence value was defined as the penetration depth (Carp et al., 2004). The penetration depths and simulated photon paths were visualized with spatial sensitivity profiles.

3. Results

3.1. System overview

The developed measurement system (device under test, DUT) consists of a main data acquisition (DAQ) unit and two external sensor units. The DAQ unit is used for interfacing with the sensors as well as capturing and storing the data. The two sensors house the optical components along with the analog and digital circuitry needed for capturing the signals. The sensors are attached to the skin using a custom biocompatible sticker. The system is depicted in Fig. 2.

3.2. Tissue–light interaction simulation

3.2.1. Penetration depth

The aim of the tissue–light interaction simulation was to study the penetration depths of different wavelengths in our measurement setup. All three wavelengths in DUT presented penetration depths of 0.5 mm. However, the voxel size limits the resolution to 0.1 mm. The Inspectra device uses four wavelengths, but to simplify the simulation steps we only selected the lowest and highest wavelengths. The penetration depths for 680 nm and 800 nm wavelengths were 6.8 mm and 6.3 mm, respectively. The difference in penetration depths is influenced by two factors: wavelength and source–detector distance. Lower wavelengths result in shallower tissue penetration, while greater source–detector distances lead to increased penetration depth, and vice versa. The fluence maps and the penetration depth analysis are shown in Fig. 3c.

3.2.2. Perfusion in impaired vascular function

We conducted additional analysis to assess the device's specificity in targeting particular tissue structures. Microvascular blood flow, and therefore oxygen perfusion, can be altered even though larger vessels work normally (Chu et al., 2020). We have classified the perfusion levels into three cases: (1) Both microvascular and macrovascular zones are working properly, (2) only macrovascular blood flow is present and (3) no blood flow is present in either zone. These are depicted in Fig. 3b. In order to simulate the different cases, we had to modify the properties of each layer in the tissue model depicted in Fig. 3a. Starting from the surface of the skin, the layers from papillary dermis up to reticular dermis were assumed to have microvascular vessels while deep blood net dermis and the subcutis were assumed to contain macrovascular vessels. The three cases were simulated by modifying μ_a, μ_s, g of whole blood at each layer. Each case was simulated for 467 nm, 584 nm and 592 nm resulting in nine simulation runs, shown in Supplementary table Appendix A. The total energy received by the detector was calculated and cases 2 and 3 are shown as percentages relative to case 1. In wavelength 467 nm the energy increased by 5.9%, while 592 nm decreased by 6.9% in cases 2 and 3 compared to case 1. This corresponds to the differences in HbO_2/Hhb absorption spectra. The isosbestic wavelength 584 nm showed an increase of 1.1%. Majority of the back-scattering happens already in the top layers of the skin, stratum corneum and living epidermis, where there is no blood flow. This means that the part of the signal affected by oxygen saturation is indeed fairly small. The results support the hypothesis that the DUT measures microvascular perfusion and is unaffected by hemodynamics in the deeper layers of the skin.

3.3. In vitro experiments

We performed *in vitro* experiments with three aims: (i) to verify the DUT's capability of measuring StO_2, (ii) calibrate the DUT and (iii) analyze uncertainties of individual device characteristics. The measurements were performed using a liquid phantom that mimics human tissue. The setup is shown in Fig. 4 A total of 4 measurements, each involving a deoxygenation process, were performed both with the DUT and the VIS–NIR spectrometer. The measurement setup is shown in Fig. 4a. Approximately 25 min of data were recorded for each measurement. The results show a gradual decrease in StO_2, followed by a period where most of the HbO_2 has been converted into Hhb. Mean StO_2 at

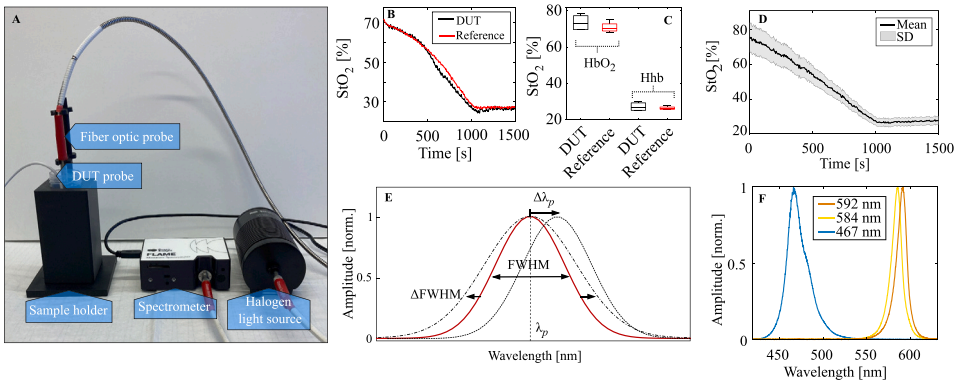

Fig. 4. *In vitro* experimentation and simulation. (a) Liquid tissue phantom experimentation setup. (b) Example of a deoxygenation measurement taken with DUT and the VIS–NIR spectrometer. (c) Box plots showing the 4 deoxygenation measurements from oxygen-rich (HbO_2) and deoxygenated (HHb) blood. CV_{DUT}: 7.5%, CV_{Ref}: 4.1% (d) Simulated effect of variation of LED characteristics to StO_2 values when computed using the proposed algorithm. (e) Variation in the spectral properties (λ_p and FWHM). (f) Spectra of the LEDs measured with a VIS–NIR spectrometer.

the start of the measurement was 71.4 StO_2-% and 26.3 StO_2-% at the end. Coefficient of variation (CV) was 7.5% and 4.1% for DUT and the reference respectively. Both DUT and VIS–NIR spectrometer exhibited similar responses during the deoxygenation process. Root mean square error (RMSE) between the two devices was 3.9 StO_2-%.

3.4. StO_2 algorithm and calibration

In order to derive actual StO_2 values from the raw ADC data, we need to calculate the optical densities (OD) for each wavelength and normalize them. Wavelengths 467 nm and 592 nm exhibit different magnitudes of change between HbO_2 and HHb and need to be accounted for. This is done by parameters ε_1 and ε_2 that are computed from their respective extinction coefficients. Since the wavelength 584 nm is very close to an isosbestic point, only one value is used. The extinction coefficients ϵ for HbO_2 and HHb at each wavelength were taken from Prahl (1999).

$$\varepsilon_1 = \left(\frac{\epsilon^{584}_{\text{oxy}}}{\epsilon^{467}_{\text{oxy}} - \epsilon^{467}_{\text{deoxy}}} \right), \varepsilon_2 = \left(\frac{\epsilon^{584}_{\text{oxy}}}{\epsilon^{592}_{\text{deoxy}} - \epsilon^{592}_{\text{oxy}}} \right) \tag{5}$$

White reference was recorded using a diffuse reflectance target. OD is a continuous variable obtained for each wavelength from raw ADC values by:

$$OD^{\lambda} = \log_{10} \left(\frac{I_0}{I} \right)^{\lambda} \tag{6}$$

where I_0 is the white reference intensity, and I is the measured intensity at the desired wavelength λ (Kleiser et al., 2018).

For computing StO_2 values we applied a custom algorithm that uses all λ_p of the three LEDs and the normalizing parameters ε_1 and ε_2:

$$StO_2^{\text{dut}} = a \frac{\varepsilon_1 OD^{467} - OD^{584}}{\varepsilon_2 OD^{592} - OD^{584}} + b \tag{7}$$

Calibration coefficients $a = 89.5$ and $b = -17.7$ are derived from *in vitro* experiments by performing a linear fit that translates the values obtained from DUT to the corresponding values measured by the VIS–NIR spectrometer.

3.5. Uncertainty of device characteristics

We studied the effect of manufacturing tolerances and temperature to the LED characteristics and its subsequent effect on StO_2 measurement accuracy. We used a sample VIS–NIR spectrometer measurement shown in Fig. 4b for the simulation and selected the wavelengths used in DUT.

LED manufacturers often specify a tolerance of how much the peak wavelength (λ_p) of the LED can diverge from the nominal value. We used LEDs with a tolerance of ±1 nm at λ_p specified by the manufacturers.

Temperature specific optical characteristics were included in the simulation. Previous studies show that a shift in λ_p is observed as a function of semiconductor junction temperature (Chhajed et al., 2005). Temperature has also been shown to affect the width of the spectrum expressed in Full Width at Half Maximum (FWHM). Table A.3 describes the characteristics linked to each LED used. Since the source study did not include the exact wavelengths used in this study, we applied blue LED characteristics to the 467 nm LED and green LED characteristics to the other two. For the simulation, the values were rounded to the nearest wavelength according to the resolution of the VIS–NIR spectrometer. The temperature was varied between 35 °C and 45 °C corresponding to the natural range of skin temperature.

The effect of tolerances in the instrumentation setup were also assessed. The component with the highest significance to the TIA output is the feedback resistor. We used a resistor with a tolerance of ±1%. The gain of the TIA is proportional to the value of the feedback resistor. Error caused by the operational amplifier was considered negligible. We added the gain error to the simulation by varying the measured ADC values by ±1%.

The simulation was performed by randomly varying the above-mentioned parameters using uniform distribution, with a resolution of 0.2 nm. This is depicted in Fig. 4. This resulted in an array of values representing the mean and width of each wavelength. In order to mimic the spectral shape of the LED, a weighed average using normal distribution was used. These values were then applied to the measured spectral data and StO_2 was computed using Eq. (7) and the simulation was run 500 times with varying input parameters for each wavelength using the Monte Carlo method.

We performed sensitivity analysis using one-factor-at-a-time method, where each parameter was assumed to have independent effect on the output. The individual effects are reported as the difference between the maximal and minimal changes averaged over the measurement. The total change in StO_2 ($\Delta StO_2^{\text{total}}$) is a combination of manufacturing tolerance of λ_p (ΔStO_2^{i}), temperature effect on λ_p (ΔStO_2^{j}), temperature effect on FWHM (ΔStO_2^{k}) and the variation in the gain of TIA (ΔStO_2^{l}):

$$\begin{aligned} \Delta StO_2^{\text{total}} &= \Delta StO_2^{i} + \Delta StO_2^{j} + \Delta StO_2^{k} + \Delta StO_2^{l} \\ &= 18.0\% + 1.2\% + 1.1\% + 1.1 \times 10^{-14}\,\% \\ &\approx 20.2\% \end{aligned} \tag{8}$$

The results show that the uncertainty of the system components is dominated by the variation in the characteristics of the LEDs on the

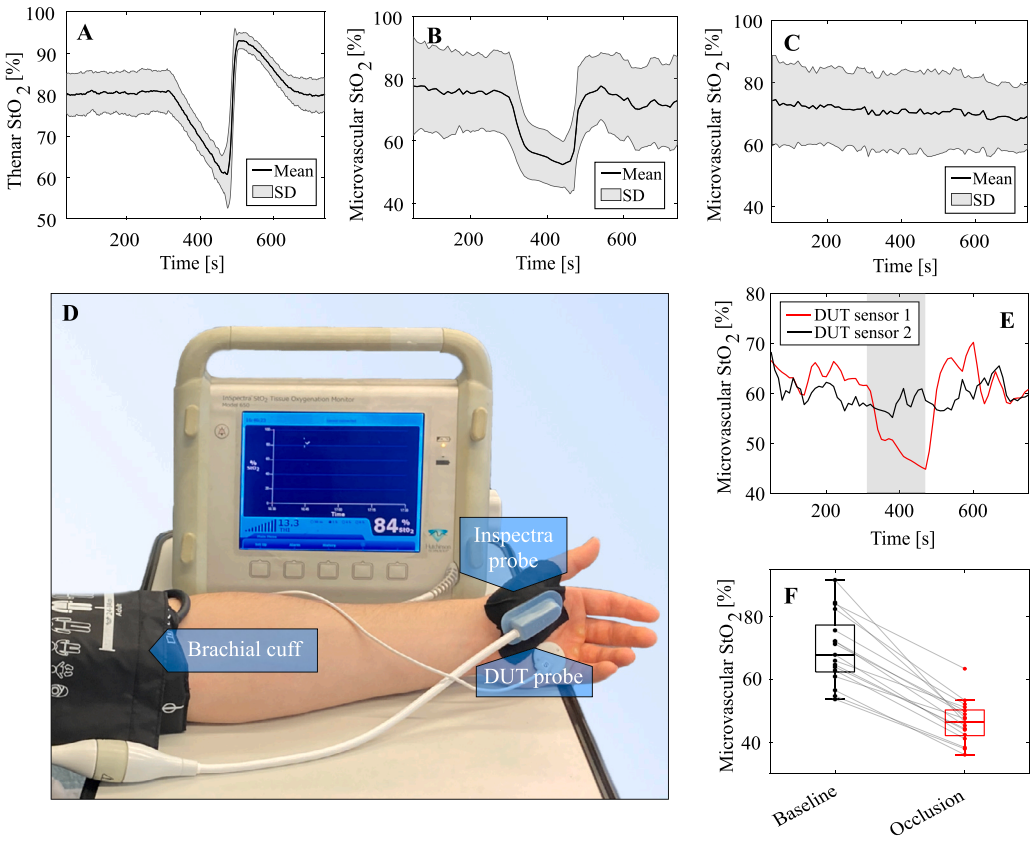

Fig. 5. Results from the human study including a total of 17 measurements from 6 subjects. (a) StO_2 measured from the thenar eminence recorded from the reference device (CV: 10.2%). (b) Microvascular StO_2 measured from the occluded hand (CV: 20.5%) and (c) from the unaffected hand (CV: 17.2%). (d) Brachial occlusion experimentation setup. An arm cuff is used to occlude the brachial artery for a period of approximately 2.5 min. The response is measured using both the DUT and a reference device (Hutchinson InSpectra 650). The other DUT sensor was placed on the contra-lateral hand. (e) Example measurement with the brachial occlusion period highlighted. (f) Paired box plot showing the difference in StO_2 during baseline and brachial occlusion, measured by DUT.

emitting side and not the tolerances in the detector side electronics. The most significant factor was the manufacturing tolerance of λ_p, while the change in TIA gain was negligible. The reason for TIA having a minimal effect is that the system is multiplexed meaning that the same amplifier is used for reading the optical signal from all wavelengths. This ensures that any possible variation in the TIA output is the same in all wavelengths.

The effect of variation in LED characteristics is shown in Fig. 4. The simulation results show that the variation between two devices can be as high as 42 StO_2-% in the worst-case scenario, with 95% confidence interval of 1.5 StO_2-%. This shows that the selection of the components is indeed critical. However, an important finding of the simulation is that despite the change, the actual shape of the StO_2 curve during deoxygenation remains the same. This indicates that majority of the spectral energies of the LEDs remain within their neighboring isosbestic points, ensuring that the direction of change in the HbO_2-HHb absorption spectra remains unaffected.

3.6. Brachial occlusion measurements

To evaluate the capability of the system to detect dynamic changes in StO_2 *in vivo*, we performed brachial occlusion measurements. In order to induce a change in StO_2 *in vivo* we performed brachial occlusion measurements resulting in a total of 17 measurements. Brachial occlusion and the assessment of post-occlusive reactive hyperemia (PORH) are commonly used to assess microvascular function (Weerts et al., 2022). Here, we refer to the reference Inspectra device measurements as thenar StO_2 and those of DUT as microvascular StO_2, since the two effectively measure different parts of the vasculature. Each measurement consists of a baseline period, brachial occlusion and a recovery period, showing the effect of PORH. Intra-subject variation was calculated for all subjects by calculating the SD between measurements at each time point. Accordingly, SD for intra-subject variation was 2.0 StO_2-% (CV: 2.6%), 5.9 StO_2-% (CV: 8.5%) and 4.4 StO_2-% (CV: 6.0%). After starting the occlusion at 300 s, a decrease in StO_2 was perceived in both thenar and microvascular StO_2. In thenar StO_2, the decrease was linear until the cuff was released, while DUT exhibited a converging decrease. The magnitude of the drop in StO_2 during occlusion were similar: 19.2 StO_2-% for the reference device and 23.4 StO_2-% for DUT. In contrast, the overshoot after the cuff release was significantly higher in the reference device measurement (12.5 StO_2-% vs 1.5 StO_2-%) during PORH. The results of the brachial occlusion measurements are shown in Table Table 1.

The results from DUT and Inspectra device cannot be directly compared, since while both measure StO_2, they do it so from different tissue layers. Yet, they are both capable of detecting decreasing oxygen saturation caused by local ischemia. The Inspectra device has previously been used to successfully record StO_2 during brachial occlusion (Lee et al., 2015). In this study, we used it to visualize the phenomenon rather than performing calibration or direct comparison with the DUT. Comparing the StO_2 readings from DUT and Inspectra, DUT showed lower baseline values: 76.0 StO_2-% (CV: 17.4%) and 72.4 StO_2-% (CV: 17.6%) vs. 80.5 StO_2-% (CV: 6.3%). These findings are supported by the literature, since microvascular StO_2 has been reported to be lower than the values measured from deeper tissues. Additionally, baseline StO_2 was computed at the beginning of each measurement using the VIS–NIR spectrometer resulting in a mean of 70.9 StO_2-% (CV: 9.2%) and intra-subject SD was 4.6 StO_2-% (CV: 6.5%). The results from the brachial occlusion measurements are depicted in Fig. 5 and Supplementary Table A.3.

3.7. Stability

We analyzed the system's capability to take long measurements by taking two test measurements. One measurement was taken with both probes measuring a white diffuse target for a duration of approximately 20 h. No noticeable drift was detected in the individual LED channels as seen in Supplementary Figure A.7. To verify the stability of the device in a real use environment, we took proof-of-concept measurement from a postoperative patient that lasted approximately 60 h. The measurement is shown in Supplementary Figure A.8. Mean ± SD for both sensors are 58.1 ± 4.1 StO_2-% and 54.7 ± 4.1 StO_2-%, respectively. At the beginning of the measurement sensor 2 exhibits some artifacts. This is likely caused by compression of the sensor due to the patient resting on it. In addition, we recorded StO_2 during different activities/positions including laying in a supine position, laying on the right side, laying on the left side, sitting and walking. For each subject, the mean and CV were calculated for each activity. These values were then averaged across all subjects, resulting in a group-level mean and CV for each activity. An example measurement is shown in Supplementary Figure A.9. While supine position and laying on right and left sides gave similar mean values of 74.4, 75.3 and 74.2 StO_2-%, walking and sitting resulted in lower means of 69.4 and 69.8 StO_2-%, respectively. As CV quantifies variability during an activity, walking exhibits the highest susceptibility to noise, with CV of 3.6% compared to 2.1% in supine position. The results are shown in Supplementary Table A.2.

4. Discussion

The capability of the proposed system to measure StO_2 was comprehensively evaluated using *in vitro*, *in vivo*, and simulation studies. The results of the simulation study show that the light in DUT penetrates the epidermis and reaches the top layers of the dermis, populated by microcircular vessels, such as capillaries, arterioles and venules. This suggests that the StO_2 signal from DUT originates from capillary and partly arteriolar circulation. In contrast, the reference device probes deeper tissues, reaching the subcutis where larger arteries are located and its StO_2 signal is likely a combination of shallow and deep circulation oxygenation. This makes direct comparison of the two devices unreasonable.

An interesting observation in our study was the difference in overshoot following occlusion cuff release between the Inspectra system and DUT. This is likely due to the different tissue layers targeted by the two devices. Similar results have previously been reported (Kanick et al., 2019). The higher wavelengths in Inspectra are able to probe both arterial and arteriolar blood, where the majority of vasodilation occurs. On the other hand, capillary blood flow is less affected by this. Compartmentalized models have been developed to assess the effect of reactive hyperemia at different parts of the circulation (Coccarelli and Nelson, 2023). What makes comparison even more complex is that reactive hyperemia affects both oxygen saturation and blood flow, dilating the vessels significantly. This is seen as an increase in both simultaneously.

The characteristics of the LEDs had a significant impact on StO_2 measurement accuracy. Nevertheless, the effect is reduced by using LEDs from the same manufacturing batch and further by individual calibration of the sensors. The effect of manufacturing tolerance of λ_p is controllable, since we can select the LEDs close to their nominal λ_p in the assembly process. However, temperature dependent variables introduce an unpredictable error to StO_2.

Special consideration has to be taken in selecting LED wavelengths for multiple reasons: (i) Preferably two wavelengths with opposing HbO_2-HHb absorption spectra changes should be selected and the change should be large enough. (ii) The distance between the selected wavelength and its neighboring isosbestic points, as well as the distance to the nearest isosbestic point, should be sufficiently large to account for the spectral width of the LED. (iii) The tissue penetration depths should be similar in the selected wavelengths to ensure that they probe the same tissue layer. In the case of an ischemic microvascular flap, probing deeper tissues can still detect oxygenated blood in underlying tissues even if the microcirculation in the flap itself is compromised. Furthermore, the availability of wavelengths from the manufacturers restricts the selection of the LEDs.

The experiments regarding the stability of the system support its capabilities for long-term wearable monitoring. The results from the activity study indicate that the technology provides reliable measurements across a range of external conditions. However, the level of StO_2 was observed to shift lower e.g. during walking. From this study alone, it is impossible to determine whether the change is due to the actual shift in StO_2. It has been previously reported that StO_2 is susceptible to external factors such as change in body temperature caused by heating (Davis et al., 2006; Thomsen et al., 2022). A major advantage of the dual-probe system is that baseline drift can be effectively accounted for if it occurs in both probes simultaneously. The reference signal can be subtracted from the signal from the site of interest, providing a differential measurement. For post-operative microvascular monitoring, one probe can be placed on healthy tissue to serve as a reference.

We recognize some limitations to the study. The accuracy of the proposed system largely depends on the validity of the *in vitro* calibration, which in this study could be affected by the use of bovine blood instead of human blood, and the fact that it was not certified reference material. During the *in vivo* study, we observed that baseline measurements from the VIS–NIR spectrometer were significantly influenced by the contact pressure and the angle of the probe affecting the results. Controlling these factors proved to be challenging. Furthermore, all human experiment measurements were taken from palmar tissue. The reason for this is that the reference StO_2 monitor is specifically intended for thenar measurement, yet the microvascular structure in the palm differs from the one in other cutaneous tissues.

The technology has potential to provide a cost-effective and convenient tool for postoperative monitoring. The cost of spectrometer-based instruments remains high. Specifically, the Spectros T-Stat main unit is priced at 37,500 USD, and each single-use fiber-optic probe costs 650 USD (Assistance Publique – Hôpitaux de Paris, 2016). The high cost per probe also limits the use of a healthy tissue reference. The component cost for a single probe for our device is approximately 18 USD, which can be significantly decreased with larger order sizes. We did not have access to the T-stat device which arguably would have been a valuable reference.

In addition to microvascular flap monitoring, there are other interesting applications for the technology, such as peripheral artery disease (PAD) and the assessment of hypoxia in cancerous tissue (Comerota et al., 2003; Nie et al., 2025). Additionally, impaired microvascular function has been shown to be present in the early stages of metabolic syndrome (Kraemer-Aguiar et al., 2008). Tissue oxygenation has been reported to decrease in non-insulin dependent diabetic patients with poor glycemic control (Iino et al., 1997). Fortunately, with lifestyle changes and medication, some of these conditions are reversible before they lead to adverse effects.

5. Conclusions

We developed a wearable monitoring system to measure StO_2 using discrete semiconductor optics and assessed its feasibility. The system was calibrated using a liquid tissue phantom and tested in a human study. We conducted a comparative analysis between our developed system, a commercial StO_2 monitor, and a VIS–NIR spectrometer. The *in vitro* study resulted in RMSE of 3.9 StO_2-% between the devices. *In vivo* baseline recordings resulted in 80.5, 76.0, 71.7 and 70.9 StO_2-% for the commercial StO_2 monitor, our device from separate hands and the VIS–NIR spectrometer, respectively. We confirmed the specific tissue layers targeted by our monitoring system through simulations of

Table 1
Results of the *in vivo* measurements. The occlusion was performed on the left hand. The results are shown as StO_2-% (CV).

Device	Hand	Baseline	Occlusion	Overshoot	SD, Intra-Subj.
Inspectra 650	L	80.5 (6.3%)	61.3 (10.3%)	93.0 (2.1%)	2.0 (2.6%)
DUT sensor 1	L	76.0 (17.4%)	52.6 (14.3%)	77.5 (14.0%)	5.9 (8.5%)
DUT sensor 2	R	71.7 (17.6%)	N/A	N/A	4.4 (6.0%)
VIS–NIR spectrometer	R	70.9 (9.2%)	N/A	N/A	4.6 (6.5%)

tissue–light interaction. This study helped us understand how the light from the LEDs interacts with various tissue layers, providing essential information to optimize sensor performance and accuracy. Addressing the challenges posed by LED variances and sensor calibration has shown to be critical in improving the accuracy of the measurements. Finally, we did a real use case demonstration of the device in a clinical setting. The results of the study are promising and pave the way for the development of low-cost portable microvascular monitoring.

A major limitation of the study is that the clinical reference monitor is designed primarily to measure systemic StO_2, rather than localized microvascular tissue oxygenation. Future work includes integrating the device into existing patient monitoring systems in the hospital freeing healthcare professionals from frequent manual assessment of tissue vitality. Further technical work includes enabling wireless communication and applying the StO_2 algorithm on the device itself.

CRediT authorship contribution statement

Tuukka Panula: Conceptualization, Data curation, Investigation, Methodology, Writing – original draft, Writing – review & editing. **Inka Mustajoki:** Data curation, Formal analysis, Writing – original draft. **Tomi Jaakola:** Investigation, Writing – original draft. **Tarja Niemi:** Conceptualization, Writing – original draft, Writing – review & editing. **Matti Kaisti:** Conceptualization, Writing – review & editing, Writing – original draft.

Declaration of competing interest

The authors declare the following financial interests/personal relationships which may be considered as potential competing interests: Matti Kaisti reports financial support was provided by European Research Council. If there are other authors, they declare that they have no known competing financial interests or personal relationships that could have appeared to influence the work reported in this paper.

Acknowledgments

This study has received funding from the European Union's Horizon Europe research and innovation programme under grant agreement No. 101115492.

Appendix A. Supplementary data

Supplementary material related to this article can be found online at https://doi.org/10.1016/j.bios.2025.118163.

Data availability

The data that support the findings of this study are available from the corresponding author upon reasonable request.

References

Assistance Publique – Hôpitaux de Paris, 2016. Spectros T-stat visible light spectroscopy acute intestinal ischemia. Online, URL https://cedit.aphp.fr/spectros-t-stat-visible-light-spectroscopy-acute-intestinal-ischemia/. (Accessed: 4 September 2025).

Bashkatov, A.N., Genina, E.A., Tuchin, V.V., Altshuler, G.B., Yaroslavsky, I.V., 2008. Monte Carlo study of skin optical clearing to enhance light penetration in the tissue: implications for photodynamic therapy of acne vulgaris. In: Shcherbakov, I.A., Myllylä, R., Priezzhev, A.V., Kinnunen, M., Pustovoy, V.I., Kirillin, M.Y., Popov, A.P. (Eds.), In: Advanced Laser Technologies 2007, vol. 7022, SPIE, International Society for Optics and Photonics, 702209. http://dx.doi.org/10.1117/12.803909.

Benaron, D.A., Parachikov, I.H., Cheong, W.-F., Friedland, S., Duckworth, J.L., Otten, D.M., Rubinsky, B.E., Horchner, U.B., Kermit, E.L., Liu, F.W., Levinson, C.J., Murphy, A.L., Price, J.W., Talmi, Y., Weersing, J.P., 2003. In: Chance, B., Alfano, R.R., Tromberg, B.J., Tamura, M., Sevick-Muraca, E.M. (Eds.), Quantitative clinical nonpulsatile and localized visible light oximeter: design of the T-Stat tissue oximeter. San Jose, CA, p. 355. http://dx.doi.org/10.1117/12.488596.

Benaron, D.A., Parachikov, I.H., Friedland, S., Soetikno, R., Brock-Utne, J., Van Der Starre, P.J., Nezhat, C., Terris, M.K., Maxim, P.G., Carson, J.J., et al., 2004. Continuous, noninvasive, and localized microvascular tissue oximetry using visible light spectroscopy. Anesthesiology 100 (6), 1469–1475.

Berthelot, M., Henry, F.P., Hunter, J., Leff, D., Wood, S., Jallali, N., Dex, E., Lysakova, L., Lo, B., Yang, G.-Z., 2019. Pervasive wearable device for free tissue transfer monitoring based on advanced data analysis: clinical study report. J. Biomed. Opt. 24 (6), 067001–067001.

Carp, S.A., Prahl, S.A., Venugopalan, V., 2004. Radiative transport in the delta-p 1 approximation: accuracy of fluence rate and optical penetration depth predictions in turbid semi-infinite media. J. Biomed. Opt. 9 (3), 632–647.

Chae, M.P., Rozen, W.M., Whitaker, I.S., Chubb, D., Grinsell, D., Ashton, M.W., Hunter-Smith, D.J., Lineaweaver, W.C., 2015. Current evidence for postoperative monitoring of microvascular free flaps: a systematic review. Ann. Plast. Surg. 74 (5), 621–632.

Chhajed, S., Xi, Y., Li, Y.-L., Gessmann, T., Schubert, E., 2005. Influence of junction temperature on chromaticity and color-rendering properties of trichromatic white-light sources based on light-emitting diodes. J. Appl. Phys. 97 (5).

Chu, E.A., Byrne, P.J., Odland, R.M., Goding, Jr., G.S., 2020. Skin flap physiology and wound healing. In: Flint, P.W., Haughey, B.H., Lund, V.J., Robbins, K.T., Thomas, J.R., Lesperance, M.M., Francis, H.W. (Eds.), Cummings Otolaryngology: Head and Neck Surgery, Seventh ed. Elsevier, Philadelphia, PA, pp. 1064–1080.

Coccarelli, A., Nelson, M.D., 2023. Modeling reactive hyperemia to better understand and assess microvascular function: A review of techniques. Ann. Biomed. Eng. 51 (3), 479–492.

Comerota, A.J., Throm, R.C., Kelly, P., Jaff, M., 2003. Tissue (muscle) oxygen saturation (StO2): a new measure of symptomatic lower-extremity arterial disease. J. Vasc. Surg. 38 (4), 724–729.

Dat, A.D., Loh, I.W., Bruscino-Raiola, F., 2017. Free-flap salvage: muscle only versus skin paddle–an Australian experience. ANZ J. Surg. 87 (12), 1040–1043.

Davis, S.L., Fadel, P.J., Cui, J., Thomas, G.D., Crandall, C.G., 2006. Skin blood flow influences near-infrared spectroscopy-derived measurements of tissue oxygenation during heat stress. J. Appl. Physiol. 100 (1), 221–224.

Fang, Q., Boas, D.A., 2009. Monte Carlo simulation of photon migration in 3D turbid media accelerated by graphics processing units. Opt. Express 17 (22), 20178–20190. http://dx.doi.org/10.1364/OE.17.020178, URL https://opg.optica.org/oe/abstract.cfm?URI=oe-17-22-20178.

Feuer, D.S., Handberg, E.M., Mehrad, B., Wei, J., Merz, C.N.B., Pepine, C.J., Keeley, E.C., 2022. Microvascular dysfunction as a systemic disease: a review of the evidence. Am. J. Med. 135 (9), 1059–1068.

Finlayson, L., Barnard, I.R., McMillan, L., Ibbotson, S.H., Brown, C.T.A., Eadie, E., Wood, K., 2022. Depth penetration of light into skin as a function of wavelength from 200 to 1000 nm. Photochem. Photobiol. 98 (4), 974–981.

Gade, J., Greisen, G., 2016. New porcine test-model reveals remarkable differences between algorithms for spectrophotometrical haemoglobin saturation measurements with VLS. Physiol. Meas. 37 (9), 1624–1635. http://dx.doi.org/10.1088/0967-3334/37/9/1624, URL https://iopscience.iop.org/article/10.1088/0967-3334/37/9/1624.

Iino, K., Yoshinari, M., Doi, Y., Shinohara, N., Iwase, M., Fujishima, M., 1997. Reduced tissue oxygenation and its reversibility by glycemic control in diabetic patients. Diabetes Res. Clin. Pract. 34 (3), 163–168.

Jubran, A., 1999. Pulse oximetry. Crit. Care 3, 1–7.

Kanick, S.C., Schneider, P.A., Klitzman, B., Wisniewski, N.A., Rebrin, K., 2019. Continuous monitoring of interstitial tissue oxygen using subcutaneous oxygen microsensors: In vivo characterization in healthy volunteers. Microvasc. Res. 124, 6–18.

Kleiser, S., Ostojic, D., Andresen, B., Nasseri, N., Isler, H., Scholkmann, F., Karen, T., Greisen, G., Wolf, M., 2018. Comparison of tissue oximeters on a liquid phantom with adjustable optical properties: an extension. Biomed. Opt. Express 9 (1), 86. http://dx.doi.org/10.1364/BOE.9.000086, URL https://opg.optica.org/abstract.cfm?URI=boe-9-1-86.

Knoefel, W.T., Kollias, N., Rattner, D.W., Nishioka, N.S., Warshaw, A.L., 1996. Reflectance spectroscopy of pancreatic microcirculation. J. Appl. Physiol. 80 (1), 116–123. http://dx.doi.org/10.1152/jappl.1996.80.1.116, URL https://www.physiology.org/doi/10.1152/jappl.1996.80.1.116.

Kraemer-Aguiar, L.G., Laflor, C.M., Bouskela, E., 2008. Skin microcirculatory dysfunction is already present in normoglycemic subjects with metabolic syndrome. Metabolism 57 (12), 1740–1746.

Lee, J.-H., Park, Y.-H., Kim, H.-S., Kim, J.-T., 2015. Comparison of two devices using near-infrared spectroscopy for the measurement of tissue oxygenation during a vascular occlusion test in healthy volunteers (INVOS® vs. InSpectra™). J. Clin. Monit. Comput. 29, 271–278.

Moreno-Oyervides, A., Díaz-Ojeda, L., Bonilla-Manrique, O.E., Bonastre-Juliá, J., Largo-Aramburu, C., Acedo, P., Martín-Mateos, P., 2023. Design and testing of an optical instrument for skin flap monitoring. Sci. Rep. 13 (1), 16778.

Nasseri, N., Kleiser, S., Wolf, U., Wolf, M., 2018. Tissue oximetry by diffusive reflective visible light spectroscopy: Comparison of algorithms and their robustness. J. Biophotonics 11 (9), e201700367. http://dx.doi.org/10.1002/jbio.201700367, URL https://onlinelibrary.wiley.com/doi/10.1002/jbio.201700367.

Nie, R., Jia, Q., Li, Y., Yan, C., Liu, X., Tao, Y., Zhang, J., Li, P., Huang, W., 2025. Implantable biophotonic device for wirelessly cancer real-time monitoring and modulable treatment. Adv. Sci. 2503778.

Pickett, J., Amoroso, P., Nield, D., Jones, D., 1997. Pulse oximetry and PPG measurements in plastic surgery. In: Proceedings of the 19th Annual International Conference of the IEEE Engineering in Medicine and Biology Society.'Magnificent Milestones and Emerging Opportunities in Medical Engineering'(Cat. No. 97CH36136), vol. 5, IEEE, pp. 2330–2332.

Prahl, S., 1999. Tabulated molar extinction coefficient for hemoglobin in water. URL https://omlc.org/spectra/hemoglobin/summary.html. (Accessed: 25 February 2025).

Prahl, S.A., Keijzer, M., Jacques, S.L., Welch, A.J., 1989. A Monte Carlo model of light propagation in tissue. In: Müller, G.J., Sliney, D.H. (Eds.), SPIE Proceedings of Dosimetry of Laser Radiation in Medicine and Biology, vol. IS 5. pp. 102–111.

Sirkiä, J.-P., Panula, T., Kaisti, M., 2023. Tonometric multi-wavelength photoplethysmography for studying the cutaneous microvasculature of the fingertip. IEEE Trans. Instrum. Meas. 72, 1–13. http://dx.doi.org/10.1109/TIM.2023.3293873.

Sonmezoglu, S., Fineman, J.R., Maltepe, E., Maharbiz, M.M., 2021. Monitoring deep-tissue oxygenation with a millimeter-scale ultrasonic implant. Nature Biotechnol. 39 (7), 855–864.

Strain, W.D., Paldánius, P., 2018. Diabetes, cardiovascular disease and the microcirculation. Cardiovasc. Diabetol. 17, 1–10.

Thomsen, A., Saalmann, M., Nicolay, N., Grosu, A., Vaupel, P., 2022. Temperature profiles and oxygenation status in human skin and subcutis upon thermography-controlled wIRA-hyperthermia. pp. 69–80, Water-filtered Infrared A (wIRA) Irradiation: From Research to Clinical Settings.

Tomioka, Y., Sekino, M., Gu, J., Kurita, M., Yamashita, S., Miyamoto, S., Iida, T., Kanayama, K., Yoshimura, K., Nakagawa, M., et al., 2022. Wearable, wireless, multi-sensor device for monitoring tissue circulation after free-tissue transplantation: a multicentre clinical trial. Sci. Rep. 12 (1), 16532.

Wang, L., Jacques, S.L., Zheng, L., 1995. MCML—Monte Carlo modeling of light transport in multi-layered tissues. Comput. Methods Programs Biomed. 47 (2), 131–146. http://dx.doi.org/10.1016/0169-2607(95)01640-F, URL https://www.sciencedirect.com/science/article/pii/016926079501640F.

Weerts, J., Mourmans, S.G., Barandiaran Aizpurua, A., Schroen, B.L., Knackstedt, C., Eringa, E., Houben, A.J., van Empel, V.P., 2022. The role of systemic microvascular dysfunction in heart failure with preserved ejection fraction. Biomolecules 12 (2), 278.

Yan, S., Fang, Q., 2020. Hybrid mesh and voxel based Monte Carlo algorithm for accurate and efficient photon transport modeling in complex bio-tissues. Biomed. Opt. Express 11 (11), 6262–6270. http://dx.doi.org/10.1364/BOE.409468, URL https://opg.optica.org/boe/abstract.cfm?URI=boe-11-11-6262.

Yu, L., Nina-Paravecino, F., Kaeli, D.R., Fang, Q., 2018. Scalable and massively parallel Monte Carlo photon transport simulations for heterogeneous computing platforms. J. Biomed. Opt. 23 (1), 010504. http://dx.doi.org/10.1117/1.JBO.23.1.010504.